

Circuit Modeling of 3D Cells to Design Versatile Full-Metal Polarizers

Carlos Molero *Member, IEEE* and María García-Vigueras *Member, IEEE*

Abstract—An original mechanism is here proposed to achieve polarization conversion from linear to circular with the use of full-metal polarizing screens. Such screens are self-supported and conceived from the periodic arrangement of 3D unit-cells. They are built from sections of rectangular waveguides operating below cutoff frequency and loaded with slotted discontinuities. The polarizer operates in transmission: the discontinuities are responsible for both its high return losses and the conversion of the impinging linear polarization to circular. Two types of 3D-cells are presented, both of them are analyzed and designed through equivalent circuit models. These models have been thoroughly built in order to capture all the phenomena underlying the discontinuities' behavior. The characterization of the first cell is fully done analytically whereas the second cell needs reduced help from a full-wave solver. Furthermore, the circuit models allow simple design guidelines to be identified for this type of polarizer. Two designs are performed operating in Ka-band, proving that an extension of the operation bandwidth (axial ratio and S_{11}) to 11% is possible by employing the second cell.

Index Terms—3D-unit cells, analytical circuit modeling, circular polarization, metallic polarizer in transmission.

I. INTRODUCTION

THE conception of directive radiating systems for modern satellite communications is facing several bottlenecks, one of them related to the generation of circular polarization (CP) [1]–[7]. The most extensive solution consists in the integration of waveguide polarizers within the beamforming network (BFN) and before the radiating elements (recent examples can be found in [2], [6], [8]). Typical polarizing components are implemented in dual-polarized waveguides (supporting two degenerate modes) which are loaded with discontinuities or perturbations, such as stepped septums, ridges, irises, or corrugated grooves [1]–[3], [9]–[11]. The design strategy consists in obtaining the required 90° phase shift between the two signals and high return loss (RL) for both polarizations. In this context, compactness and simplicity are commonly traded-off with the use of dielectric materials [8], [12]. Though full-metal components are commonly preferred for spacecraft applications, they are also normally bulky and

often imply an increase of the array beamforming network (BFN) complexity.

Lately, the development of an alternative solution consisting in the use of external polarizing screens is attracting significant attention, since it allows compact illuminating antenna architectures with linear polarization (LP) to be considered [4], [5], [7], [13], [14]. The relevance of this solution is even greater when the generation of CP from the considered radiating elements is not evident (for example, in the case of radiation from parallel-plate waveguide BFNs [15], [16]). Polarizing sheets can be conceived to operate in reflection mode [4], [5] or in transmission mode [7], [13], [14], [17]–[19], the latter being the most compact solution. Seminal works on external polarizers were based on the anisotropy of meander line gratings [19]–[23]. More generally, the polarizer design is tackled basing on the dispersion of a periodic surface when illuminated by a 45° -slant impinging wave, where the periodicity should be sub-wavelength in order to avoid the appearance of grating lobes (GL) [5]. These polarizers are implemented using printed circuit board (PCB) technology, involving sometimes the use of multiple PCB layers when operating in transmission, thus becoming less attractive for spaceborne antennas. All cited examples are based on periodic bi-dimensional environments, which allow to be understood and characterized with the help of intuitive circuit models (CMs) [24]. Many examples can be found where specific CMs are built to design polarizers. For example, in [7] and [25], the authors report different design techniques based exclusively on classical circuit analysis. In the patents [26], [27], the authors also describe their complex proposals with the help of equivalent CMs.

An original approach is proposed here to design full-metal and self-supported polarizing screens operating in transmission. By self-supporting it is understood that the architecture does not need any additional elements to be built (such as foam, or any backing elements). To the authors' best knowledge, such an objective has not yet been addressed, and it is not straightforward since metallic architectures tend to present high RL to the impinging electromagnetic waves (thus reflecting backwards most of the energy). In order to pursue a self-supported polarizer, an array of metallic cells can be considered. When choosing its periodicity, a trade-off appears between the avoidance of GL (where sub-wavelength cells are preferred) and the matching to the impinging wave (since those lattices are highly reactive). To face this challenge, the strategy followed by the authors is the use of three-dimensional (3D) cells which are built from sections of metallic squared waveguides operating below cutoff frequency which are loaded

Manuscript received May 30th, 2018; revised Oct. 27th, 2018; accepted Jan. 20th, 2019.

C. Molero and M. García-Vigueras are with the Institut d'Electronique et de Télécommunications de Rennes, UMR CNRS 6164, INSA Rennes, France (email: carlos.molero-jimenez@insa-rennes.fr; maria.garcia-vigueras@insa-rennes.fr).

This work has been supported by Rennes Métropole with the funds AIS 17C0481 and Region Bretagne with the contract SAD 2016 9637.

This paper is an extended version from the 2018 IMS International Microwave Conference, Philadelphia, PA 10-15 June 2018.

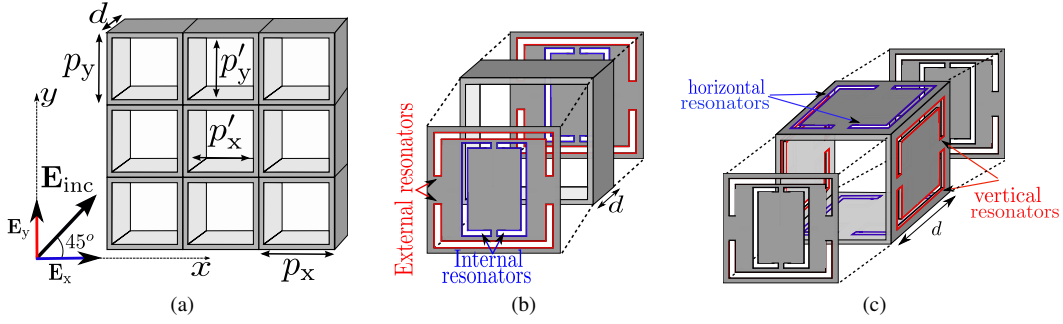


Fig. 1: Building full-metal self-supported polarizers. (a) Illumination by a 45°-slant plane-wave of the elementary bi-dimensional structure. Exploded view of 3D unit-cells: (b) simple polarizer topology, (c) structure with enhanced performance.

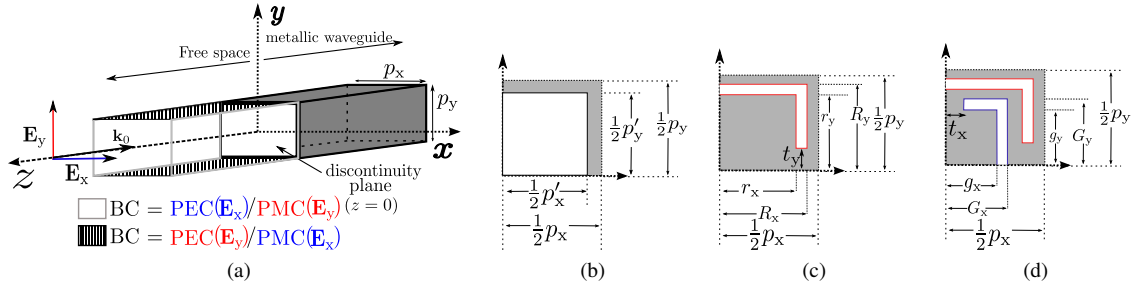


Fig. 2: (a) General scenario employed to model the discontinuity between free space and a rectangular metallic waveguide. Possible perforations considered in the discontinuity plane (only one quarter is depicted due to symmetry): (b) empty aperture of length p'_x , (c) folded slot with average length L , (d) folded dual slot with average lengths of external and internal resonators L_{ext} and L_{int} , respectively. The average lengths can be calculated as $L = L_{\text{ext}} = \frac{1}{2}(R_x + r_x)\frac{1}{2}(R_y + r_y) - t_y$ and $L_{\text{int}} = \frac{1}{2}(G_x + g_x) + \frac{1}{2}(G_y - g_y) - t_x$.

with slot-based discontinuities. Such cells are inspired by the operation mechanism of evanescent-mode waveguide filters [28], and their basic topology has been briefly presented in [29] for the first time. Various types of slot discontinuities load the 3D-cells; novel and fully analytical CMs are proposed here for the first time to characterize all of them extending the work in previously reported in [29]. By properly adjusting the location, geometry, orientation and dimensions of such discontinuities, it is not only possible to enhance transmission through the cells, but also to control their phase response and to synthesize conversion between impinging linear polarization to circular. The CMs promote a precise understanding of how the 3D-cells operate and enable us to propose design guidelines for the efficient design of polarizers.

The CMs proposed here are based on a modal decomposition at both sides of a discontinuity. This approach was first presented in [30] to explain the appearance of extraordinary transmission through perforated arrays. More recently, it has been proven that a fully analytical characterization of periodic surfaces is possible as long as the field distribution in the perforation (or the current profile in the scatterer) is also known analytically. The following examples have been addressed: rectangular and annular apertures [31], [32] and meander-line gratings [14]. The key assumption in those examples is to consider that the known analytical profile does not change within the frequency band of interest. Very recently it has been proven possible

the consideration of multiple resonances in the scatterer (or higher order resonances in the same scatterer) by cleverly identifying the CM corresponding topology [33]. In the present contribution, the geometry of the perforations loading the cell should allow a first resonance before the appearance of GL. Additionally, in order to address polarization conversion, compound perforations are chosen that allow independent interactions with the horizontally and vertically polarized waves. To this aim, folded coupled rings have been chosen, which have the additional benefit of being self-supported.

This manuscript is organized as follows. Section II describes the topology of the different 3D-cells that are considered to build the polarizers. Section III presents the analytical CMs to characterize the different discontinuities loading the cells. Section IV explains how to build the CM and the guidelines to design a basic polarizer operating at 30 GHz. An enhancement of this polarizer is pursued in Section V, aiming at broader operation bandwidth. Finally, the conclusion of the work is provided in Section VI.

II. 3D UNIT-CELLS: REACTIVE WAVEGUIDES LOADED WITH DISCONTINUITIES

The architecture of the proposed self-supported polarizers is shown in Fig. 1, and consists in a doubly-periodic arrangement of 3D unit-cells. Depicted in Fig. 1a, the elementary structure is an array of square waveguide sections of length d operating below cutoff frequency (being both p_x and p_y smaller than

half a wavelength). The considered illumination is a 45° -slant plane wave impinging normally, thus allowing to describe the scattering scenario by considering two in-phase incident plane waves with equal amplitudes and orthogonal polarisations, i. e. an horizontal component E_x and an vertical one E_y (also depicted in Fig. 1a).

The reactive structure in Fig. 1a does not allow full transmission of impinging waves, since its lattice is smaller than half a wavelength. However, and in analogy to the operation of evanescent-mode waveguide filters [28], by loading the unit-cells in Fig. 1a with resonant discontinuities is it possible to assure full transmission within a certain frequency band. In a first step, the configuration of Fig. 1b is considered to build a simple polarizer, where the cell presents discontinuities both at its input and output walls. The topology depicted in Fig. 1c considers additional perforations in the cell lateral walls, and it will be analyzed in a second step when aiming at polarizer with enhanced performance.

The discontinuities loading the cells correspond to compound resonators built from couples of folded slots. Such a geometry has been chosen carefully in order to comply with the following conditions. Firstly, their lowest resonance appears below the appearance of GL. Secondly, they preserve the symmetry of the structure (thus avoiding cross-pol excitation). Thirdly, they allow direct interaction with E_x and E_y . Finally, they preserve the self-supporting character of the structure. As highlighted in Fig. 1b, the couples of slots loading the input and output walls are named as *external* or *internal* resonators, and their average lengths are respectively L_{ext} and L_{int} . The same way, the resonators placed in the lateral walls of Fig. 1c are denoted as *vertical* or *horizontal*, and their respective average length is L_{ver} and L_{hor} . As it will be accurately justified in the following sections, the *internal* and the *horizontal* resonators are intended to interact mainly with the E_x component, whereas the *external* and the *vertical* allow the interaction with E_y .

In order to explain the operation of the 3D-cells, an intermediate step is carried out to understand precisely the behavior of all the discontinuities that are present in Fig. 1. The general scenario depicted in Fig. 2a is considered, where a plane wave (with horizontal or vertical polarization) propagating in free space impinges on a discontinuity that is followed by an infinite metallic rectangular waveguide of section $p_x \times p_y$. As shown Fig. 2a, depending on its polarization, the impinging wave faces perfect electric/magnetic conductor (PEC/PMC) boundary conditions at the edges of the cell. The different types of discontinuities that are considered are shown in Figs. 2b-2d; only one quarter of them is necessary to the analysis due to symmetry. A single and rectangular aperture of length $p'_x \times p'_y$ is considered in Fig. 2b, a single folded slot with average length L in Fig. 2c and finally, a dual resonator built from the combination of an external and an internal folded slots of average length L_{ext} and L_{int} , respectively.

The discontinuities are firstly modeled Section III by equivalent CMs following a fully analytical approach. These CMs are then used in Sections IV and V to build CMs for the 3D-cells in Fig. 1b and Fig. 1c, respectively.

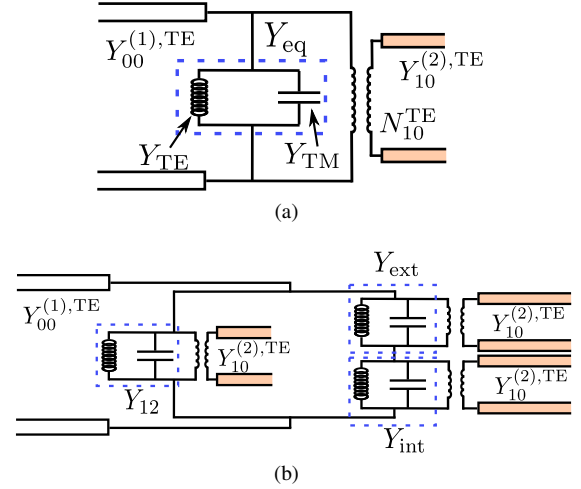


Fig. 3: Analytical circuits proposed to model the excitation of the scenarios described in Fig. 2. Characterization of discontinuities with (a) single resonance (the examples in Fig. 2b and Fig. 2c) and (b) dual resonance (Fig. 2d).

III. ANALYTICAL CHARACTERIZATION OF DISCONTINUITIES

The present section is focused in the development of analytical CMs to characterize all the discontinuity problems shown in Fig. 2. As sketched in Fig. 2a, the discontinuity plane is created in the interface between free space (the leftmost medium) denoted by region (1), and a metallic rectangular waveguide, denoted as region (2). The rigorous methodology presented in [33] is here employed as the basis to obtain the CMs, which consists on a modal decomposition at both sides the discontinuity. The main requirement of such an approach is the analytical expression of the electric field profile at the discontinuity plane, $\mathbf{E}_{type}^{TE/TM}$. Consequently, the main assumption is that this profile does not vary with the frequency (at least, not in the frequency of interest). In this context, the considered discontinuities can be classified into two groups. The first one includes the examples in Fig. 2b and Fig. 2c, where the electric-field profile can be analytically approximated by a single function. They can be identified as a single-aperture problem, and they are characterized by the CM in Fig. 3a. The second group concerns the example in Fig. 2d and it can be regarded as a two-apertures discontinuity problem. This case needs two functions, (one per aperture), included in a global profile $\mathbf{E}_{dual}^{TE/TM}$ and its equivalent CM is depicted in Fig. 3b. **In every case, analytical functions are proposed for the electric-field distribution in the discontinuity. This functions have been built by inspecting the eigen modal patterns satisfying the conditions imposed by the excitation, as done in [14], [34].**

A. Circuit model for single-aperture discontinuities

The general approach to characterize discontinuities of the first group is described in [31]. The equivalent admittance

analytically deduced in such a reference is the following:

$$Y_{\text{eq}} = \sum'_{\forall n,m} [Y_{nm}^{\text{TE,(1)}} |N_{nm,\text{type}}^{\text{TE,(1)}}|^2 + Y_{nm}^{\text{TM,(1)}} |N_{nm,\text{type}}^{\text{TM,(1)}}|^2] + \sum'_{\forall n,m} [Y_{nm}^{\text{TE,(2)}} |N_{nm,\text{type}}^{\text{TE,(2)}}|^2 + Y_{nm}^{\text{TM,(2)}} |N_{nm,\text{type}}^{\text{TM,(2)}}|^2]. \quad (1)$$

This expression involves two infinite summations. The leftmost summation contains the modal admittances $Y_{nm}^{\text{TE/TM,(1)}}$ of all higher-order modal solutions of order n, m , both of TE and TM nature existing in the region of incidence named as (1). The symbol ' at the top of the summation indicates that the incident mode (usually the fundamental one with order $n, m=(0,0)$) is excluded. The rightmost summation involves the modal admittances in the region behind the discontinuity, named as region (2). Again, the symbol ' indicates that the fundamental mode in this region, usually the TE_{10} mode, is excluded from the summation. The expressions of the modal admittances are identical in both cases, and given by

$$Y_{nm}^{\text{TE,(i)}} = \frac{\beta_{nm}^{(i)}}{\omega \mu_0} \quad (2)$$

$$Y_{nm}^{\text{TM,(i)}} = \frac{\varepsilon_r^{(i)} \varepsilon_0 \omega}{\beta_{nm}^{(i)}} \quad (3)$$

with $\varepsilon_r^{(i)}$ being the relative permittivity in regions $i = 1, 2$ and

$$\beta_{nm}^{(i)} = \sqrt{\varepsilon_r^{(i)} k_0^2 - k_{nm}^{(i)2}} \quad (4)$$

the propagation constant of a mode of order n, m , where we identify the wavenumber in vacuum is k_0 and the cutoff wavenumber of a given mode $k_{nm}^{(i)}$. Finally, the terms $N_{nm,\text{type}}^{\text{TE/TM,(i)}}$ in Eq.(1) can be seen as transformers that account for the amount of coupling between the electric field excited at the discontinuity plane and a particular mode. As explained in [31], this term can be expressed as

$$N_{nm,\text{type}}^{\text{TE/TM,(i)}} = \frac{\int_{\Omega} \mathbf{E}_{\text{type}}^{\text{TE/TM}} \cdot [\mathbf{E}_{nm}^{\text{TE/TM,(i)}}]^* d\Omega}{\int_{\Omega} \mathbf{E}_{\text{type}}^{\text{TE/TM}} \cdot [\mathbf{E}_{00}^{\text{TE/TM,(1)}}]^* d\Omega} \quad (5)$$

where $\mathbf{E}_{nm}^{\text{TE/TM,(i)}}$ and $\mathbf{E}_{00}^{\text{TE/TM,(1)}}$ denote the electric field profile of the mode under consideration (either TE or TM, of order nm), and the incident one (which is the fundamental, of order $n = m = 0$) respectively. The symbol Ω denotes the integration domain covered by the geometry of the aperture. The mathematical expressions of the modal profiles supported at each region are written in the Appendix. $\mathbf{E}_{\text{type}}^{\text{TE/TM}}$ represents the electric field distribution at the discontinuity plane. The indexes TE and TM denote the polarizing nature of the impinging field that excites the discontinuity. The subscript 'type' refers to the type of discontinuity we are considering. Finally, the superindex "*" denotes refers to the complex conjugate of the function.

The discontinuity of Fig.2b is the simplest one, and it consists of the simple junction of the waveguides and can be seen as a wide rectangular aperture of dimensions $p'_x x p'_y$.

An appropriate $\mathbf{E}_{\text{type}}^{\text{TE/TM}}$ that describes how the electric field is distributed in this case is the one associated to the $\text{TE}_{10}^{(2)}$ mode (i.e., of order $n, m = (1,0)$). In spite of being an approximation, this profile works correctly at frequencies below the appearance of GL because this mode is the fundamental one inside the waveguide. Furthermore, under normal incidence the next modes supported by the metallic waveguide are the $\text{TE}_{12}^{(2)}/\text{TM}_{12}^{(2)}$, whose cutoff frequencies are far above the onset of the $\text{TE}_{10}^{(2)}$. If vertical polarization is impinging on the structure (mode $\text{TE}_{00}^{(1)}$), the $\mathbf{E}_{\text{type}}^{\text{TE/TM}}$ field profile at the discontinuity is analytically expressed as

$$\mathbf{E}_{\text{ap}}^{\text{TE}} = \cos(k_{10}^{(2)} x) \hat{y} \quad (6)$$

with $k_{10}^{(2)} = \frac{\pi}{p'_x}$ being the cutoff wavenumber of the mode TE_{10} , the superscript TE denoting the incident polarization and the subscript 'ap' denoting the type of discontinuity, in this case *aperture*-type. If the opposite polarization is impinging, say TM with the electric field along x , the field profile could be rewritten as

$$\mathbf{E}_{\text{ap}}^{\text{TM}} = \cos(k_{01}^{(2)} y) \hat{x} \quad (7)$$

with $k_{01}^{(2)} = \frac{\pi}{p'_y}$ and where the superscript TM denotes the polarizing nature of the incident wave.

Moving on to consider the folded-slot discontinuity in Fig.2c, the appropriate field profile to be used is not associated with a particular modal field distribution but with the resonances supported by the folded slot. A sensible approximation is to use the profile of the lowest-order resonance. Its electric-field distribution is strongly dependent on the incident polarization. For vertical polarization (namely TE incidence), the lowest-order resonant mode resembles a sort of cosinusoidal variation distributed along the whole folded slot. The folded slot can actually be divided into three sections: An horizontal and a vertical section, and a corner where they both converge. The cosinusoidal field distribution can therefore be split as follows:

$$\mathbf{E}_{\text{ext}}^{\text{TE}}(x, y) = \mathbf{E}_{\text{ext}}^{\text{TE,hor}}(x, y) + \mathbf{E}_{\text{ext}}^{\text{TE,ver}}(x, y) + \mathbf{E}_{\text{ext}}^{\text{TE,cor}}(x, y) \quad (8)$$

$$\mathbf{E}_{\text{ext,hor}}^{\text{TE}}(x, y) = \cos(q_1 x) \hat{y} \quad (9)$$

$$\mathbf{E}_{\text{ext,ver}}^{\text{TE}}(x, y) = \cos\left(q_1 \frac{1}{2} [R_x + R_y + r_x + r_y - y]\right) \hat{x} \quad (10)$$

$$\mathbf{E}_{\text{ext,cor}}^{\text{TE}}(x, y) = \mathbf{E}_{\text{ext,hor}}^{\text{TE}}(r_x, y) \frac{R_x - x}{R_x - r_x} + \mathbf{E}_{\text{ext,ver}}^{\text{TE}}(x, r_y) \frac{R_y - y}{R_y - r_y} \quad (11)$$

with $q_1 = \pi/L$ being the wavenumber associated with the resonant mode and the the subindexes 'hor', 'ver', 'cor' labelling the horizontal, vertical and corner sections, respectively. The superindex TE refers to the nature of the incident field. The subscript 'ext' indicates that the slot under consideration is the external one. This nomenclature make more sense in next section where it is necessary to distinguish between the external and internal slot resonators. In this section we proceed assuming that the internal slot has been

removed. Note that we have modeled the field along the folded slot according to the strategy reported in [14], where a sinusoidal surface-current modulation was adapted to the shape of a metallic meander-line.

For the opposite incident polarization, where the electric field is polarized along x , the boundary conditions of the parallel-plate region are inverted. This rotation affects drastically the field distribution inside the slots. Now, the lowest-order resonant profile is the well-known one of second order (which resonates when L is approximately λ), and it can be modeled by the following sine modulation, split into three parts:

$$\mathbf{E}_{\text{ext}}^{\text{TM}}(x, y) = \mathbf{E}_{\text{ext}}^{\text{TM,hor}}(x, y) + \mathbf{E}_{\text{ext}}^{\text{TM,ver}}(x, y) + \mathbf{E}_{\text{ext}}^{\text{TM,cor}}(x, y) \quad (12)$$

$$\mathbf{E}_{\text{ext,hor}}^{\text{TM}}(x, y) = \sin(q_2[x - t_x])\hat{\mathbf{y}} \quad (13)$$

$$\mathbf{E}_{\text{ext,ver}}^{\text{TM}}(x, y) = \sin\left(\frac{1}{2}q_2[R_x + R_y + r_x + r_y - y - 2t_x]\right)\hat{\mathbf{x}} \quad (14)$$

$$\mathbf{E}_{\text{ext,cor}}^{\text{TM}}(x, y) = \mathbf{E}_{\text{ext,hor}}^{\text{TM}}(r_x, y) \frac{R_x - x}{R_x - r_x} + \mathbf{E}_{\text{ext,ver}}^{\text{TM}}(x, r_y) \frac{R_y - y}{R_y - r_y} \quad (15)$$

where $q_2 = 2\pi/L$. The superindex 'TM' refers to the polarization of the incident wave

The values of the transformers $N_{nm,\text{type}}^{\text{TE/TM},(i)}$ can be calculated analytically from the field distribution. The complete calculations are detailed in the Appendix. The admittance expression in (1) is topologically represented in the circuit of Fig. 3a. It includes an infinite summation of modal admittances, translated to the circuit language as an infinite parallel connection of elements. The admittances of TM nature can be grouped into a single global term, which from the circuit point of view provides the so-called capacitive contribution of the discontinuity. Similarly, all the elements of TE nature are grouped into another single term providing the corresponding inductive contribution:

$$Y_{\text{TM}} = \sum_{\forall n,m} \left[Y_{nm}^{\text{TM},(1)} |N_{nm,\text{type}}^{\text{TM},(1)}|^2 + Y_{nm}^{\text{TM},(2)} |N_{nm,\text{type}}^{\text{TM},(2)}|^2 \right] \quad (16)$$

$$Y_{\text{TE}} = \sum_{\forall n,m} \left[Y_{nm}^{\text{TE},(1)} |N_{nm,\text{type}}^{\text{TE},(1)}|^2 + Y_{nm}^{\text{TE},(2)} |N_{nm,\text{type}}^{\text{TE},(2)}|^2 \right]. \quad (17)$$

Those admittances are parallel connected, forming a sort of LC -tank. Since the TE_{10} mode is the fundamental one inside the waveguide, we take it out the summation in (16). This mode is usually not far from being launched at the frequency range of operation, having a dynamical frequency dependence. The summations therefore involves modes far from their cutoff, so that they have a quasi-static character allowing the summation in (16) to reduce their complexity [31]. A global view of the resulting circuit is sketched in Fig. 3a. In addition to the aforementioned admittances, the two transmission lines appearing describe the propagation of the incident mode on the one hand, with characteristic admittance $Y_{00}^{\text{TE},(1)}$ (for TM incidence, we just have to interchange the

$Y_{00}^{\text{TE},(1)}$ by $Y_{00}^{\text{TM},(1)}$); and the propagation (or exponential decay) of the TE_{10} field beyond the discontinuity, with characteristic admittance $Y_{10}^{\text{TE},(2)}$. It is worth remarking that this latter line is connected to the rest of the circuit through a transformer with turns ratio $N_{10,\text{type}}^{\text{TE},(2)}$, that accounts for the amplitude of the mode.

B. Circuit model for two-apertures discontinuities

An analytical CM can also be deduced for discontinuity planes that can be interpreted as a two-apertures problem such as the discontinuity type in Fig. 2d. In [33] a rigorous and mathematical methodology is reported for periodic structures consisting on a two double-slot discontinuity. The field profile at the discontinuity can now be expressed as follows:

$$\mathbf{E}_{\text{dual}}^{\text{TE/TM}} = A\mathbf{E}_{\text{ext}}^{\text{TE/TM}} + B\mathbf{E}_{\text{int}}^{\text{TE/TM}}, \quad (18)$$

where A and B are constant values accounting for the degree of excitation of each profile, and $\mathbf{E}_{\text{ext}}^{\text{TE/TM}}$, $\mathbf{E}_{\text{int}}^{\text{TE/TM}}$ are actually the field profiles at each of the slot resonators taking place at the discontinuity. The label 'ext' denotes the field profile for the external resonator. This field profile was defined in (8) and (12) for TE and TM incidence respectively. The label 'int' denotes the field profile at the internal resonator. For the sake of simplicity this profile has not been explicitly shown in this report since its definition is analogous to the profile of the external resonator. Note that the orientation of this second slot resonator is rotated 90° with respect to the external one. The mathematical expression for its field profile needs to be readjusted. For TE incidence, the proper profile would now be that defined in (12) but interchanging the variables x and y and the corresponding delimitations of the corners. For TM incidence the corresponding field profile is that in (8), also with the variables x and y , and the delimitations of the corners interchanged.

As explained in [33], a field profile of this kind naturally leads to a CM whose topology is that presented in Fig. 3b. The equivalent admittance is formed by two different branches connected in parallel. The leftmost branch accounts for the possible coupling between both different folded slots. This coupling is taken into account through the admittance Y_{12} , formally expressed as:

$$Y_{12} = \sum_{\forall n,m} \left[Y_{nm}^{\text{TE},(1)} N_{nm,\text{ext}}^{\text{TE},(1)} N_{nm,\text{int}}^{\text{TE},(1)} + Y_{nm}^{\text{TE},(2)} N_{nm,\text{ext}}^{\text{TE},(2)} N_{nm,\text{int}}^{\text{TE},(2)} \right] + \sum_{\forall n,m} \left[Y_{nm}^{\text{TM},(1)} N_{nm,\text{ext}}^{\text{TM},(1)} N_{nm,\text{int}}^{\text{TM},(1)} + Y_{nm}^{\text{TM},(2)} N_{nm,\text{ext}}^{\text{TM},(2)} N_{nm,\text{int}}^{\text{TM},(2)} \right]. \quad (19)$$

The incident wave and the $\text{TE}_{10}^{(2)}$ mode are excluded from this summation. The transformers $N_{nm,\text{ext}}^{\text{TE/TM},(i)}$ and $N_{nm,\text{int}}^{\text{TE/TM},(i)}$ are calculated considering again the corresponding field profile (external or internal) at the discontinuity.

The second branch (on the right) in Fig. 3b is formed by a series connection of two different parallel tanks. Each of them describes the phenomenology associated with each of the folded slots independently. The global admittance of these tanks is expressed as:

$$Y_{\text{ext/int}} = \hat{Y}_{\text{ext/int}} - Y_{12} \quad (20)$$

with

$$\hat{Y}_{\text{ext}} = \sum_{\forall n,m} \left[Y_{nm}^{\text{TE,(1)}} |N_{nm,\text{ext}}^{\text{TE,(1)}}|^2 + Y_{nm}^{\text{TE,(2)}} |N_{nm,\text{ext}}^{\text{TE,(2)}}|^2 \right] \quad (21)$$

$$+ \sum_{\forall n,m} \left[Y_{nm}^{\text{TM,(1)}} |N_{nm,\text{ext}}^{\text{TM,(1)}}|^2 + Y_{nm}^{\text{TM,(2)}} |N_{nm,\text{ext}}^{\text{TM,(2)}}|^2 \right] \quad (22)$$

$$\hat{Y}_{\text{int}} = \sum_{\forall n,m} \left[Y_{nm}^{\text{TE,(1)}} |N_{nm,\text{int}}^{\text{TE,(1)}}|^2 + Y_{nm}^{\text{TE,(2)}} |N_{nm,\text{int}}^{\text{TE,(2)}}|^2 \right] \quad (23)$$

$$+ \sum_{\forall n,m} \left[Y_{nm}^{\text{TM,(1)}} |N_{nm,\text{int}}^{\text{TM,(1)}}|^2 + Y_{nm}^{\text{TM,(2)}} |N_{nm,\text{int}}^{\text{TM,(2)}}|^2 \right]. \quad (24)$$

Again, the mode TE_{10} is excluded from all the summations. All the admittances of TE nature contribute inductively in (21) and (23) as well as TM admittances contribute capacitively. This is considered in the circuit in Fig. 3b by corresponding inductors and capacitors

C. Test of Discontinuities CM

A set of results has been plotted in Fig. 4 with the aim of checking the robustness of the above CMs by comparing with the results given by the full-wave solver HFSS. Each plot concerns a particular discontinuity and shows the variation of the reflection coefficient within the a certain frequency range of interest. Additionally, the color-plot insets corresponds to the considered profile $\mathbf{E}_{\text{type}}^{\text{TE/TM}}$.

In Fig. 4a vertical incidence (TE) is considered over a rectangular aperture discontinuity (type Fig. 2a). Three examples, associated with three different geometries of the discontinuity, are plotted. At lower frequencies full reflection is achieved for every example since the $\text{TE}_{10}^{(2)}$ mode is still reactive, contributing to the global reactive tank. This tendency changes once the mode becomes propagative, being those cutoff frequencies 30 GHz for a waveguide with $p'_x = p'_y = 5$ mm (results in red), and 37.5 GHz for $p'_x = p'_y = 4$ mm (results in blue). Black lines and points consider a case where the $\text{TE}_{10}^{(2)}$ mode has not been excited yet.

In Fig. 4b the discontinuity in Fig. 2b is considered under vertical excitation (TE incidence). The field profile shown in the inset is directly identified with the distribution mathematically expressed in (8). Three different geometries are again considered, each one regarding a different slot length. The waveguide size is fixed, thus being the $\text{TE}_{10}^{(2)}$ launched at the same frequency in all cases. As it could be expected, the CMs predict no transmission below this frequency in all cases. Above this point, the level of transmission depends on the length of the slot. Longer folded slots allow for higher transmission, since they are closer to resonance.

The Fig. 4c shows results for the same previous discontinuity but under horizontal incidence (TM incidence). The considered field profile shown in the inset resembles the distribution in (12). Such a resonance will not take place within the frequency interval considered. Therefore, and in contrast to the previous results, the transmission coefficient remains low after the onset of the $\text{TE}_{01}^{(2)}$ mode in the waveguide.

Finally, Fig. 4d and Fig. 4e refer to the same discontinuity under vertical (TE) and horizontal (TM) polarization, respectively. The field distribution at the discontinuity is now built from two functions. In the case of Fig. 4d, the distribution in the *external* resonator corresponds to the profile in (12) whereas the distribution in the *internal* one follows the profile (8). Similar conclusions can be extracted as in the previous cases. The abrupt variations that appear around 36 GHz in Fig. 4e correspond to the well known phase resonances [30], exhibited in FSS whose discontinuity plane is formed by several slot/apertures. It is actually the series resonance between the elements forming the second branch of the equivalent circuit in Fig. 3b.

To conclude this subsection, it is worth noting that the agreement between the CM and HFSS is very good in all cases. The CM provides very useful physical insight, it captures all possible modal onsets and resonance phenomena, thus demonstrating its dynamical character and robustness.

IV. BASIC POLARIZER DESIGN : CM & GUIDELINES

The design of a polarizer employing the 3D-cells depicted in Fig. 1b is here pursued. This cell can be seen as the interconnection of two consecutive discontinuities through a section of rectangular waveguide of length d . The CM of Fig. 5 can be used to model this scenario, and it has been intuitively built by using the model developed for such discontinuity in the previous section, shown in Fig. 3b. As it is explained in [35], this way to proceed to combine multiple discontinuities is accurate. Here we assume that both discontinuities couple to each other through the fundamental mode of the rectangular waveguide, and therefore, by the transmission lines of length d and characteristic admittance $Y_{10}^{\text{TE,(2)}}$. The frequency range of operation is such that the cavity operates below its cutoff frequency. This implies that the coupling between discontinuities is carried out by an evanescent field instead of a propagating one, following the philosophy presented for evanescent filters in [28]. At frequencies close to the resonance of the folded slots, a constructive coupling between both perforated screens is produced through the transmission line of the TE_{10} mode. As it is explained in [28], full transmission is produced thanks to the coupling of both screens, and two transmission peaks are exhibited. An even more rigorous description of such coupling would imply the interconnection of the rest of higher-order modes of the waveguide. However we have not considered this option, since this would increase dramatically the complexity of the CM without improving much its accuracy.

As explained in Section II, the considered 45° -slant wave illumination allows to consider two separate scattering problems, namely, E_x (horizontal) or E_y (vertical) excitation.

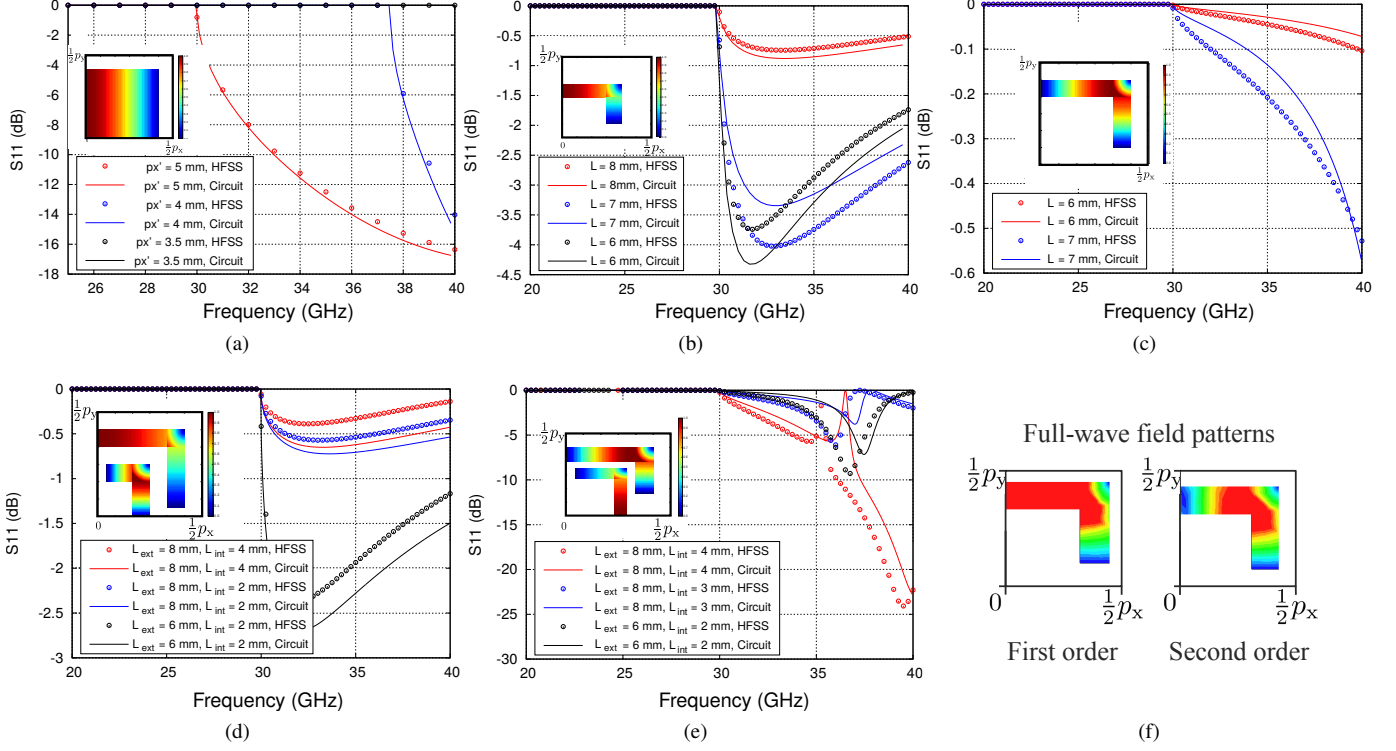


Fig. 4: Comparison between CM and HFSS reflection coefficients associated to the excitation of the discontinuities in Fig. 2. The colour-plot inset in each graph corresponds to the considered pattern of the electric field in each discontinuity $E_{\text{type}}^{TE/TM}$. (a) E_y excitation of the aperture described in Fig. 2b employing the CM in Fig. 3a. (b) and (c) display respectively E_y and E_x excitation of the folded slot described in Fig. 2c employing the CM in Fig. 3a. (d) and (e) display respectively E_y and E_x excitation of folded dual-slot described in Fig. 2d employing the CM in Fig. 3b. (f) Folded slots field patterns obtained from eigen-mode full-wave simulations. For the folded-slot cases, $p_x = p_y = 6$ mm, $p'_x = p'_y = 5$ mm.

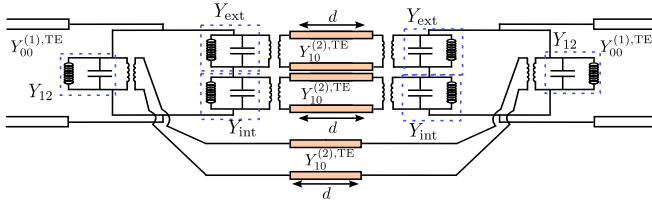


Fig. 5: Analytical CM to characterize the excitation of the 3D unit-cell in Fig. 1b considering a dual-resonance profile E_{dual} in the folded dual-slot.

Thus, two different CMs with the same topology need to be built (the specific analytical values obtained for each element in both circuits can obviously differ). The behaviour predicted by the CM for three different cells is shown in Fig. 6 (dimensions are given in the caption). In order to illustrate the procedure followed to synthesize polarization conversion, three examples are considered where only the parameter L_{int} is varied. Let's start by analyzing the magnitude of the transmission coefficient depicted in Fig. 6a. When approaching the unit-cell, E_x and E_y induce respectively the lowest-order resonance of the *internal* and the *external* resonators. The same way, the impact of the *external* and the *internal* resonators is almost negligible for the E_x and

E_y , respectively. The scattering properties of the cell are then governed by the coupling between the front and back resonant screens through the waveguide section. As shown in Fig. 6a, a transmission band is created for each polarization, formed by two peaks of full transmission as the result of the coupling of the two resonant screens. Since L_{ext} is bigger than L_{int} , the transmission band for E_y appears for lower frequencies than the one of E_x . By modifying L_{int} , it can be appreciated that the transmission band for E_x is altered, allowing for higher or lower overlapping between the transmission band for both polarizations. The impact of L_{int} in the phase response of the 3D-cell is key for the polarization conversion, as shown in Fig. 6b. Within the transmission bands for each polarization the phase of the transmission coefficient has an almost linear behavior. By tuning the value of L_{int} it is possible to synthesize a desired phase delay with one polarization with respect to the other. As pointed out in Fig. 6b, 90° delay may be obtained to achieve CP by properly adjusting the value of L_{int} . The axial ratio (AR) corresponding to each of the three examples is shown in Fig. 6c. There, it is clear that a trade-off exists between the bandwidth of the AR behavior and its maximum value within the operation band.

The results given by a commercial full-wave solver (CST) are shown in Fig. 7 considering the same case of vertical polarization included in Fig. 7a and Fig. 7b. The results given

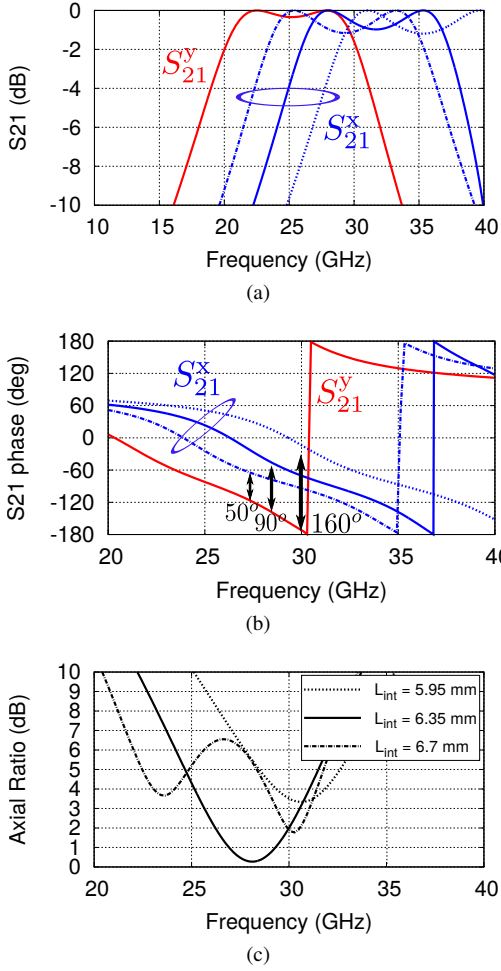


Fig. 6: Illustration of the procedure to design a polarizing 3D unit-cell using the analytical CM of Fig. 5. (a) and (b) show the magnitude and phase of the transmission coefficient S_{21}^x, S_{21}^y when illuminated by x/y -polarized waves respectively. (c) Shows the AR obtained when the cell is illuminated by a 45° -slant wave. Dimensions (in mm) are: $p_x = p_y = 6$, $p'_x = p'_y = 5$, $d = 1.75$, $L_{\text{ext}} = 7.5$.

by the CM in Fig. 5 are also shown, its agreement with CST is reasonably good, but some deviation appears in the second peak of total transmission. Some level of disagreement could be expected from this analytical CM since some assumptions have been made when building it. At this stage, the designer may opt for using directly a commercial full-wave solver to optimize the design. It is important to highlight that the analytical CM provides the user with a design that is an excellent starting point for such optimization.

A final design has been performed targeting at operation within the Ka-band (around 28 GHz), its performance and dimensions are shown in Fig. 8. The dimensions actually coincide with the example shown in Fig. 6 where good axial ratio is achieved. The matching and transmission properties are displayed in Fig. 8a, they have been computed using the

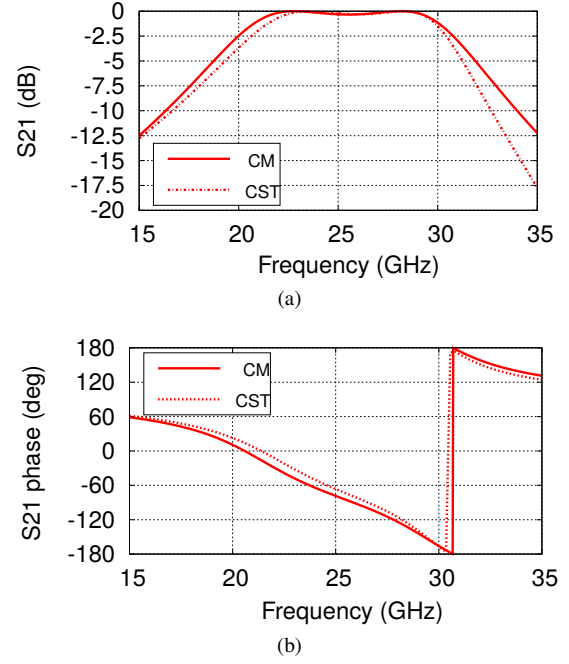


Fig. 7: Numerical comparison of the results provided by the CM and CST. Geometrical parameters: $p_x = p_y = 6$ mm, $p'_x = p'_y = 5$ mm, $d = 1.75$ mm, $L_{\text{ext}} = 7.5$ mm, $L_{\text{int}} = 6.35$ mm.

following expressions

$$S_{21}^{\text{RHCP}} = \frac{1}{2}(S_{21}^y + jS_{21}^x) \quad (25)$$

$$S_{21}^{\text{LHCP}} = \frac{1}{2}(S_{21}^y - jS_{21}^x) \quad (26)$$

$$|S_{21}| = \frac{1}{\sqrt{2}}\sqrt{|S_{21}^y|^2 + |S_{21}^x|^2}. \quad (27)$$

The AR is shown in Fig. 8a. While the band in which the AR remains 1 dB is of 8.5%, the polarizer presents a reduced matching bandwidth of 5% where the $S_{11} < -15$ dB. It can be concluded that, without performing any full-wave optimization of the CM results, a polarizer with 5% total bandwidth is obtained where the main constraint is the matching. Numerical results concerning the response of the polarizer for oblique incidence are also displayed in Fig. 8c and Fig. 8d. In particular the AR is plotted versus frequency for several incidence angles. There is not a high degradation in comparison to its behavior at normal incidence. Otherwise it is remarkable the appearance of a glitch between 26-27 GHz. This is due to the break of symmetry caused by the oblique illumination. Normal incidence preserves high symmetry on the unit cell of Fig. 1b, allowing to deal only with one quarter of it (cells in Fig. 2). Under those circumstances, the elements of a couple of folded resonator are excited in phase. Oblique incidence facilitates well-known phase resonances of narrow-band nature [33], resulting in the glitches observed in the plots. Fortunately those defects do not appear at the center of band, but at the extremes. It is worth remarking that those results have been directly obtained from CST, since the CM is conceived for normal incidence.

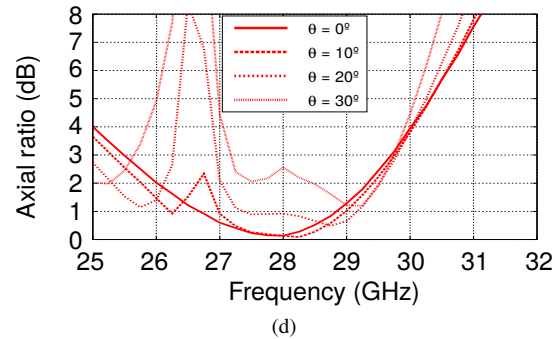
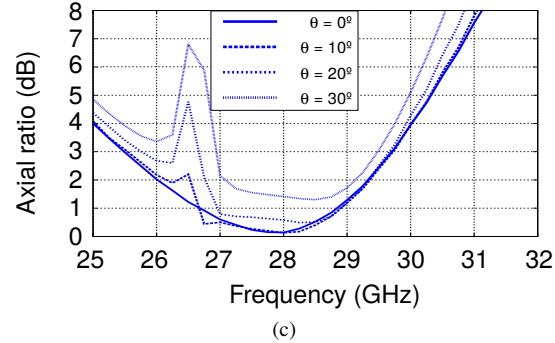
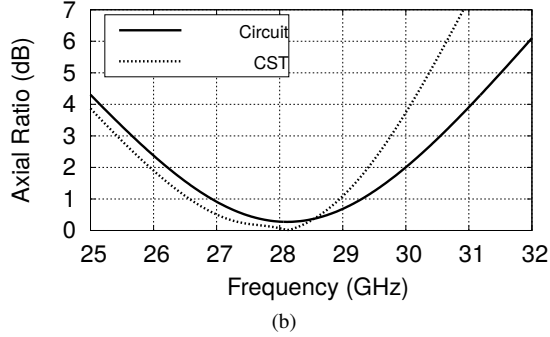
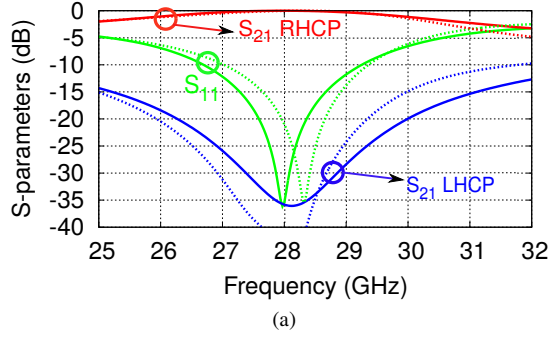


Fig. 8: Performance of polarizer designed to operate around 28 GHz. (a) Matching and transmission coefficients, comparison between CM and CST (b) Axial ratio for normal incidence, (c) Axial ratio for TE oblique incidence, (d) AR for TM oblique incidence. Geometrical parameters: $p_x = p_y = 6$ mm, $p'_x = p'_y = 5$ mm, $d = 1.75$ mm, $L_{ext} = 7.5$ mm, $L_{int} = 6.35$ mm.

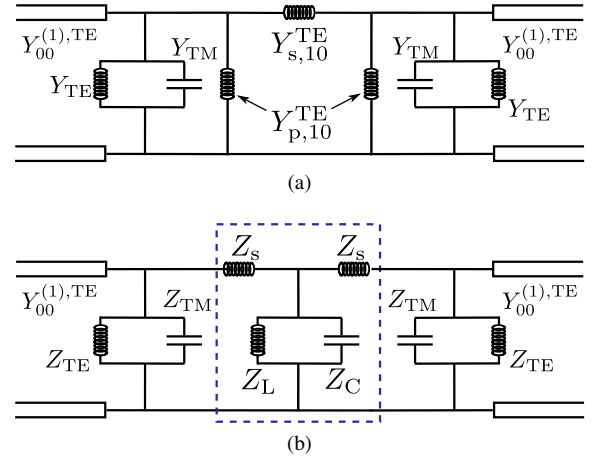


Fig. 9: (a) Simplification of the CM to characterize the excitation of the 3D unit-cell in Fig. 1b. (b) Extended CM to characterize the 3D-cell in Fig. 1c.

V. CIRCUIT MODEL FOR ENHANCED POLARIZER DESIGN

The main disadvantage of the previous polarizer stems from its narrow matching bandwidth, which spoils the total bandwidth to a 5% in spite of having 8.5% AR bandwidth. The matching bandwidth in that design is directly related to the partial overlap between the transmission bands for both vertical and horizontal polarizations. As illustrated in Fig. 6, wider overlap between passbands would be possible by adjusting L_{int} however, this would deteriorate the phase difference between outgoing signals, and consequently, also the AR.

A possible way of enlarging the operation bandwidth of the polarizer can be addressed by increasing the individual bandwidth associated with each component. This can be done by introducing an additional resonator per polarization to the unit-cell of Fig. 1c. This is precisely the role of the *vertical* and *horizontal* couples of folded slots included in the cell of Fig. 1c. The couple denoted as *vertical* strongly affects vertical polarization while not influencing the horizontal one. They are perforated at both lateral walls of the cell in order to preserve the whole symmetry of the structure. Similarly, the couples perforated in the upper and lower walls impact directly the horizontal polarization and are almost invisible to the vertical one. This way, an additional means of independent interaction has been added to the cell for each polarization : by tuning either L_{hor} or L_{ver} it is possible to add an additional and resonance to the transmission band of the horizontal and vertical polarizations, respectively.

For this new cell architecture the proposed CM is not fully analytical. The new set of resonators perforated in the waveguide walls makes the calculation of its modal fields much more complicated. To the best of the authors' knowledge no analytical solution has been proposed so far considering discontinuities that are placed in the cell longitudinal axis. Still, it is possible to propose an heuristic topology based on two reasonable approximations.

Firstly, the previous section has provided evidence that the high degree of independence between the *external/vertical*

perforations and the V/H-excitations. This fact suggests that we would still capture the main underlying phenomena of the cell in Fig. 1b by just considering the existence of the perforation perpendicular to the impinging polarization and ignoring the parallel one. This way, can simplify the dual-aperture scenario by a simpler single-aperture one, and the the CM in Fig. 5 would be simplified by the one in Fig. 9a (here, models in Fig. 3a are interconnected, and the interconnecting transmission line of the $TE_{10}^{(2)}$ mode is transformed in its equivalent π -circuit [35]). This simpler (still analytical) CM involves a loss in precision, since it only accounts for a single aperture for each polarization, but captures the main phenomena taking place within the cell (since the not accounted perforation does not present any singularity within the considered frequency regime). The LC -tanks at the input and output of Fig. 9a represent the aperture resonance, and the inductive π -topology stands for the coupling between front and back perforated screens.

Secondly, the heuristic CM in Fig. 9b is proposed as an extension of Fig. 9a, to characterized the cell in Fig. 1c. In analogy to the rest of folded slots, here it is assumed that the perforations loading the lateral walls of the cell can be represented by the additional LC -tank added in the middle of the circuit. The external tanks, namely Z_{TM} and Z_{TE} , can still be calculated by the analytical formulas given in Section III for a single-aperture problem. However, the intermediate T-circuit highlighted with a square in Fig. 9b is still unknown, and external input from a full-wave solver is required to find its numerical values. In practice, what it is here proposed, is to simulate the structure with a commercial solver at 2 frequency points, from which the values of Z_L , Z_C and Z_s can be extracted.

Some numerical results are shown in Fig. 10, where 4 different configurations of the unit cell are regarded. Only the average length of the *horizontal* resonators (L_{hor}) is modified, thus affecting only the performance of the horizontal polarization. The rest of the cell parameters are fixed for all the examples. The first remark to be made in Fig. 10a is the appearance of three peaks of full transmission in the bands of both polarizations. In the case of horizontal polarization, it can be observed how the modification of the length of the resonator allows to shift the position of the intermediate peak. As it was done in the previous section, the phase plot should be regarded in order to choose the most appropriate value of L_{hor} that provides conversion to CP. The AR curves corresponding to each of these designs are plotted in Fig. 10c. The best case corresponds to the one where $L_{hor} = 4.4$ mm since it provides the desired 90° difference between transmitted H and V-pol signals. In Fig. 10a it can be observed that now, the overlapping region between both polarizations contains two peaks of total transmission (and not only one, as it happened in the previous section). This particular case has been analyzed individually in Fig. 11. There, the S_{11} coefficient has been plotted together with the transmission coefficient associated with RHCP and LHCP. Now, the S_{11} parameters remains below -15 dB over a 14% bandwidth, which is almost three times wider than the one obtained in the previous section. The AR has also improved up to 11%. Thus, it can be concluded that

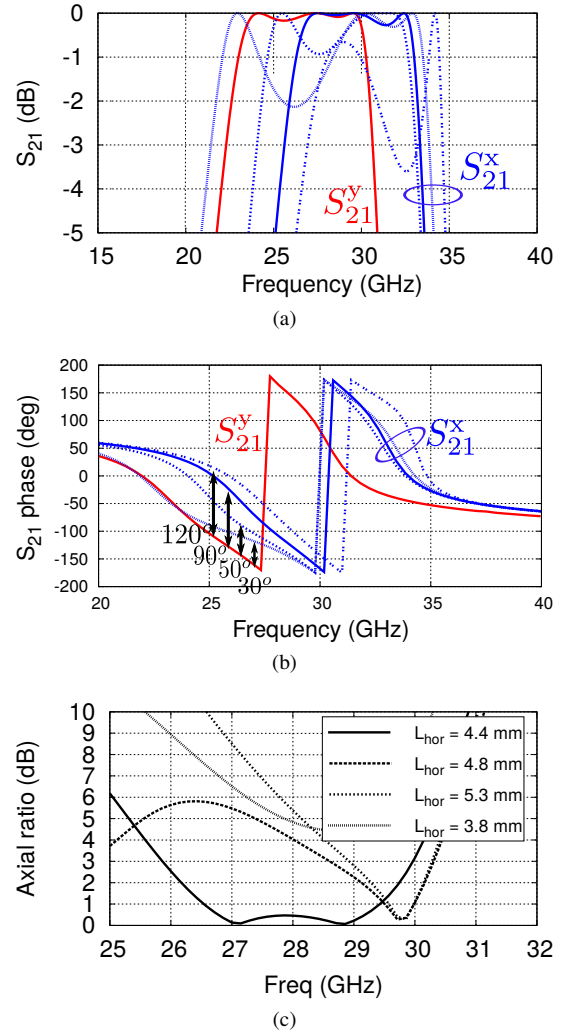


Fig. 10: Illustration of the procedure to design a polarizing 3D unit-cell using the analytical CM of Fig. 9b. (a) and (b) show the magnitude and phase of the transmission coefficient when illuminated by x/y -polarized waves. (c) Shows the AR obtained when the cell is illuminated by a 45° -slant wave. Geometrical parameters: $p_x = p_y = 6$ mm, $p'_x = p'_y = 5$ mm, $d = 1.75$ mm, $L_{ext} = 7.5$ mm, $L_{int} = 6.35$ mm, $L_{ver} = 5.5$ mm.

the total performance of the polarizer has been substantially improved. The agreement between the heuristic CM and the commercial software is very good. It is worth highlighting that this percentage of bandwidth does not overcome those achieved by other polarizers found in the literature, as [19] or [21] (neither in terms of thickness or insertion loss). The scope of this paper is not yet focused on overcoming the RF performance of other polarizers, but enabling for the first time CP conversion without the need for dielectric or any other supporting materials.

Finally, the behavior of the structure under oblique incidence is also considered in Fig. 11c and 11d. Good performance is approximately maintained up to 20° . Beyond this incidence angle, the AR is clearly deteriorated. The appearance of the peaks between 25 and 26 GHz, and between

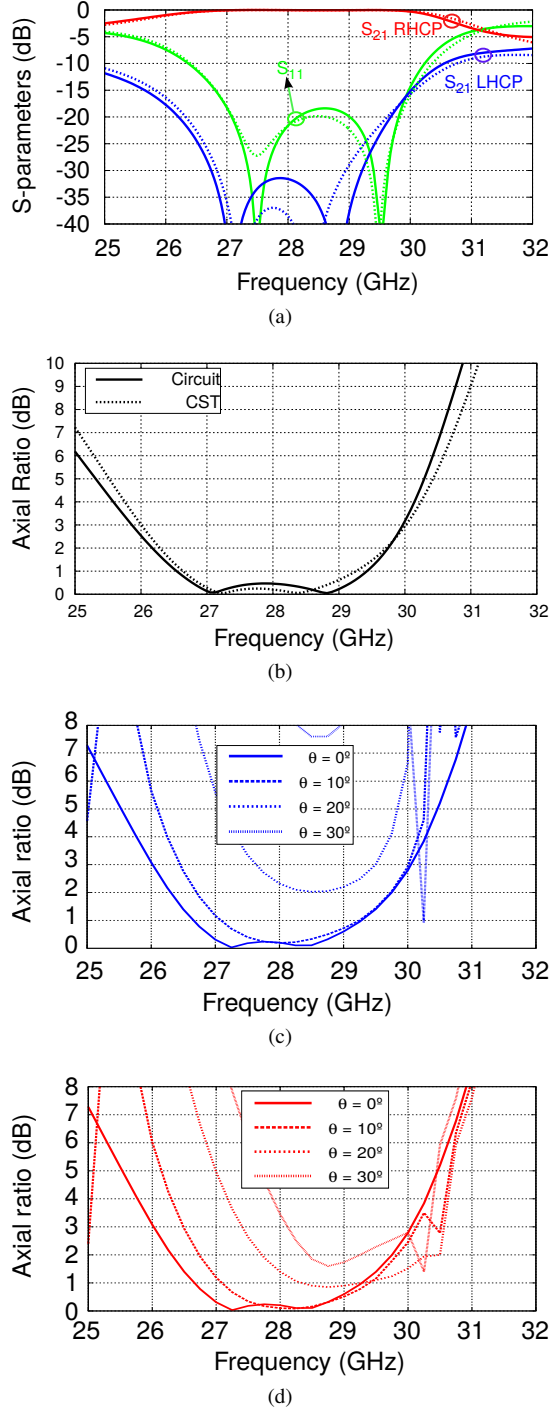


Fig. 11: Performance of a polarizer obtained by the cell in Fig. 1c, where (a) represents the scattering parameters, (b) the resulting axial ratio for normal incidence, (c) the axial ratio for TE oblique incidence, and (d) the axial ratio for TM oblique incidence. Geometrical parameters: $p_x = p_y = 6$ mm, $p'_x = p'_y = 5$ mm, $d = 1.75$ mm, $L_{\text{ext}} = 7.5$ mm, $L_{\text{int}} = 6.35$ mm, $L_{\text{ver}} = 5.5$ mm, $L_{\text{hor}} = 4.4$ mm.

30 and 31 GHz is again due to the symmetry break induced by oblique incidence (as it happened in the previous case). Those numerical results have directly been obtained from CST.

VI. CONCLUSION

This paper has addressed, for the first time, the analysis and design of full-metal polarizing surfaces operating in transmission. These periodic screens are self-supported and conceived from 3D unit-cells which combine rectangular waveguide sections and folded slot discontinuities. Analytical CMs have been proposed to model such discontinuities very accurately. Two different topologies of 3D-cells have been proposed, the second one allowing for wider operation bandwidth than the first one. The polarizing behavior of the cells has been explained thanks to the equivalent CMs.

APPENDIX

MODAL SOLUTIONS OF WAVEGUIDES AND MATHEMATICAL EXPRESSIONS OF THE MODAL TRANSFORMERS

The analytical modal solutions for each waveguide as well as the calculation of $N_{nm}^{\text{TE/TM}}$ are here shown. The modal solutions of region (1), assuming vertical normal incidence (TE incidence) are

TE MODES:

$$E_x(x, y) = \frac{k_m}{k_{nm}} \frac{2}{\sqrt{p_x p_y}} \frac{1}{\sqrt{\alpha_n \alpha_m}} \sin(k_n x) \sin(k_m y) \quad (28)$$

$$E_y(x, y) = \frac{k_n}{k_{nm}} \frac{2}{\sqrt{p_x p_y}} \frac{1}{\sqrt{\alpha_n \alpha_m}} \cos(k_n x) \cos(k_m y) \quad (29)$$

$$H_y(x, y) = Y_{nm}^{(1), \text{TE}} E_x(x, y, z) \quad (30)$$

$$H_x(x, y) = -Y_{nm}^{(1), \text{TE}} E_y(x, y, z) \quad (31)$$

$$H_z(x, y) = -j \frac{k_{nm}}{\omega \mu_0} \frac{2}{\sqrt{p_x p_y}} \frac{1}{\sqrt{\alpha_n \alpha_m}} \sin(k_n x) \cos(k_m y); \quad (32)$$

TM MODES:

$$E_x(x, y) = \frac{k_n}{k_{nm}} \frac{2}{\sqrt{p_x p_y}} \frac{1}{\sqrt{\alpha_n \alpha_m}} \sin(k_n x) \sin(k_m y) \quad (33)$$

$$E_y(x, y) = -\frac{k_m}{k_{nm}} \frac{2}{\sqrt{p_x p_y}} \frac{1}{\sqrt{\alpha_n \alpha_m}} \cos(k_n x) \cos(k_m y) \quad (34)$$

$$H_y(x, y) = Y_{nm}^{(1), \text{TM}} E_x(x, y) \quad (35)$$

$$H_x(x, y) = -Y_{nm}^{(1), \text{TM}} E_y(x, y) \quad (36)$$

$$E_z(x, y) = -j \frac{k_{nm}}{\beta_{nm}^{(1)}} \frac{2}{\sqrt{p_x p_y}} \frac{1}{\sqrt{\alpha_n \alpha_m}} \sin(k_n x) \cos(k_m y), \quad (37)$$

with

$$k_n = \frac{2n\pi}{p_x} \quad n \geq 0 \quad (38)$$

$$k_m = \frac{2m\pi}{p_y} \quad m \geq 0 \quad (39)$$

$$k_{nm} = \sqrt{k_n^2 + k_m^2} \quad (40)$$

$$\alpha_i = \begin{cases} 1 & \text{si } i = 0 \\ 1/2 & \text{si } i \neq 0 \end{cases} \quad i = n, m \quad (41)$$

For the conventional waveguide, we have exactly the same mathematical expressions for the TE and TM modes, but we have to apply some minor changes. Firstly we have to interchange p_x, p_y (period of the cell, dimensions of the waveguide in region (1)) for the internal dimensions of the metallic waveguide p'_x, p'_y . Secondly, consider explicitly the set of new definitions for the following parameters:

$$k_n = \frac{(2n+1)\pi}{p'_x} \quad n \geq 0 \quad (42)$$

$$k_m = \frac{2m\pi}{p'_y} \quad m \geq 0 \quad (43)$$

$$k_{nm} = \sqrt{k_n^2 + k_m^2} \quad (44)$$

$$\alpha_m = \begin{cases} 1 & \text{si } m = 0 \\ 1/2 & \text{si } m \neq 0 \end{cases} \quad (45)$$

$$\alpha_n = 1/2 \quad (46)$$

By using the above modal solutions and the fields at the discontinuities mathematically exposed in Sect. III, we can calculate the factors $N_{nm,type}^{TE/TM}$ associated with each of the discontinuities problems via (5). For the simple junction sketched in Fig. 2b, these factors are in the waveguide region

$$N_{nm,ext}^{TE,(1)} = \frac{2}{\sqrt{\alpha_n \alpha_m}} \frac{1}{\sqrt{p_y p_x}} \frac{1}{k_{nm}} \left(\underbrace{\Gamma_{nm} [\sin(k_m R_y) - \sin(k_m r_y)]}_{\text{Horizontal section}} \times \underbrace{\left[\frac{\sin((k_n - q_1)r_x)}{2(k_n - q_1)} + \frac{\sin((k_n + q_1)r_x)}{2(k_n + q_1)} \right]}_{\text{Horizontal section}} \right) \\ + \underbrace{\frac{\cos(q_1 r_x)}{R_x - r_x} \Gamma_{nm} [\sin(k_m R_y) - \sin(k_m r_y)]}_{\text{Corner section}} \times \underbrace{\left[\frac{-R_x}{k_n} \sin(k_n r_x) + \frac{r_x}{k_n} \sin(k_n r_x) - \frac{1}{k_n^2} (\cos(k_n R_x) - \cos(k_n r_x)) \right]}_{\text{Corner section}} \\ - \underbrace{\frac{\cos(q_1 r_x)}{R_y - r_y} \frac{1}{\Gamma_{nm}} [\cos(k_n R_x) - \cos(k_n r_x)]}_{\text{Corner section}} \times \underbrace{\left[\frac{-R_y}{k_m} (\sin(k_m R_y) - \sin(k_m r_y)) \frac{R_y}{k_m} \cos(k_m R_y)}_{\text{Corner region}} \right. \\ \left. - \frac{r_y}{k_m} \cos(k_m r_y) + \frac{1}{k_m^2} \sin(k_m R_y) - \frac{1}{k_m^2} \sin(k_m r_y) \right]}_{\text{Corner section}} \\ + \underbrace{\frac{1}{\Gamma_{nm}} [\cos(k_n R_x) - \cos(k_n r_x)]}_{\text{Vertical section}} \left[\underbrace{\frac{\cos((k_m + q_1)r_y)}{2(k_m + q_1)}}_{\text{Vertical section}} + \underbrace{\frac{\cos((k_m - q_1)r_y)}{2(k_m - q_1)} - \frac{\cos((k_m + q_1)t_y)}{2(k_m + q_1)} - \frac{\cos((k_m - q_1)t_y)}{2(k_m - q_1)}}_{\text{Vertical section}} \right] \right). \quad (51)$$

$$N_{nm,ext}^{TM,(1)} = \frac{2}{\sqrt{\alpha_n \alpha_m}} \frac{1}{\sqrt{p_y p_x}} \frac{1}{k_{nm}} \left(\underbrace{\Gamma_{nm} [\sin(k_m R_y) - \sin(k_m r_y)]}_{\text{Horizontal section}} \times \underbrace{\left[-\frac{\cos((-k_n + q_2)r_x - q_2 t_x)}{2(-k_n + q_2)} - \frac{\cos((k_n + q_2)r_x - q_2 t_x)}{2(k_n + q_2)} \right]}_{\text{Horizontal section}} \right) \\ + \underbrace{\frac{\cos(k_n t_x)}{2(-k_n + q_2)} + \frac{\cos(k_n t_x)}{2(k_n + q_2)}}_{\text{Horizontal section}} + \underbrace{\frac{\sin(q_2(r_x - t_x))}{R_x - r_x} \Gamma_{nm} [\sin(k_m R_y) - \sin(k_m r_y)]}_{\text{Corner section}} \\ \times \underbrace{\left[\frac{-R_x}{k_n} \sin(k_n r_x) + \frac{r_x}{k_n} \sin(k_n r_x) - \frac{1}{k_n^2} (\cos(k_n R_x) - \cos(k_n r_x)) \right]}_{\text{Corner section}} - \underbrace{\frac{\sin(q_2(r_x - t_x))}{R_y - r_y} \frac{1}{\Gamma_{nm}} [\cos(k_n R_x) - \cos(k_n r_x)]}_{\text{Corner section}} \times$$

(1) as follows:

$$N_{nm,ap}^{TE,(1)} = \frac{1}{4} \pi \frac{k_m}{k_{nm}} \frac{\sin(\frac{1}{2} k_m p'_y)}{\frac{1}{2} k_m p'_y} \times \quad (47)$$

$$\left(\frac{\sin(\frac{1}{2} [k_n p'_x + \pi])}{\frac{1}{2} [k_n p'_x + \pi]} + \frac{\sin(\frac{1}{2} [k_n p'_x - \pi])}{\frac{1}{2} [k_n p'_x - \pi]} \right) \quad (48)$$

$$N_{nm}^{TM,(1)} = N_{nm}^{TE,(1)} \frac{k_n}{k_m} \quad (49)$$

where we have used the field profile in (6) and the modal solutions written above. For the metallic waveguide, the only non-zero transformer is that corresponding to the $TE_{10}^{(2)}$, since its profile is identical to the one at the discontinuity. The rest of modes are orthogonal to it, so their contribution is zero. We then have

$$N_{10,ap}^{TE,(2)} = \frac{1}{2} \pi \sqrt{\frac{p_x p_y}{p'_x p'_y}} \quad (50)$$

In the case of the folded-slot discontinuities, the $N_{nm,type}^{TE/TM,(i)}$ factors are also next calculated. For the external slot, assuming TE/TM incidence, its corresponding transformer in region (1) is:

with

$$\Gamma_{nm} = \begin{cases} \Gamma_{nm} = \frac{k_n}{k_m} & \text{TE modes} \\ 1 & \text{TM modes} \end{cases} \quad (53)$$

For waveguide region (2), the expressions are analytically identical, but it is necessary to interchange the waveguide limits p_x, p_y for p'_x, p'_y , and the corresponding cutoff wavenumbers k_n, k_m, k_{nm} as well as the values of α_n, α_m . It is also worth remarking that the turns ratios associated with the internal slot are identically calculated, but after taking into account the pertinent changes mentioned above.

REFERENCES

- [1] G. Virone, R. Tascone, O. A. Peverini, G. Addamo, and R. Orta, "Combined-phase-shift waveguide polarizer," *IEEE Microwave Wireless Components Lett.*, vol. 18, no. 8, pp. 509–511, Aug 2008.
- [2] C. A. Leal-Sevillano, J. A. Ruiz-Cruz, J. R. Montejo-Garai, and J. M. Rebollar, "Dual-band bi-phase waveguide polarizer for a novel feeder network without orthomode transducer," in *2013 European Microwave Conference*, Oct 2013, pp. 593–596.
- [3] D. Schobert, C. Pfluegler, T. Thiry, P. Kohl, and M. Schneider, "A study on polarisers for satellite applications," in *GeMiC 2014; German Microwave Conference*, March 2014, pp. 1–4.
- [4] R. Orr, G. Goussetis, V. Fusco, and E. Saenz, "Linear-to-circular polarization reflector with transmission band," *IEEE Trans. Antennas Propag.*, vol. 63, no. 5, pp. 1949–1956, May 2015.
- [5] N. J. G. Fonseca and C. Mangenot, "High-performance electrically thin dual-band polarizing reflective surface for broadband satellite applications," *IEEE Trans. Antennas Propag.*, vol. 64, no. 2, pp. 640–649, Feb 2016.
- [6] F. Bongard, M. Gimersky, S. Doherty, X. Aubry, and M. Krummen, "3d-printed ka-band waveguide array antenna for mobile satcom applications," in *2017 11th European Conference on Antennas and Propagation (EUCAP)*, Paris, France, Mar. 2017.
- [7] M. Hosseini and S. V. Hum, "A circuit-driven design methodology for a circular polarizer based on modified jerusalem cross grids," *IEEE Trans. Antennas Propag.*, vol. 65, no. 10, pp. 5322–5331, Oct 2017.
- [8] A. Jensen, J. Voss, and D. L. Runyon, "Partial dielectric loaded septum polarizer," *ViaSat, Inc., US Patent 2016/0351984 A1*, May 2015.
- [9] J. Bornemann and V. A. Labay, "Ridge waveguide polarizer with finite and stepped-thickness septum," *IEEE Trans. Microw. Theory Techn.*, vol. 43, no. 8, pp. 1782–1787, Aug 1995.
- [10] J. Bornemann, S. Amari, J. Uher, and R. Vahldieck, "Analysis and design of circular ridged waveguide components," *IEEE Trans. Microw. Theory Techn.*, vol. 47, no. 3, pp. 330–335, Mar 1999.
- [11] N. Yoneda, M. Miyazaki, H. Matsumura, and M. Yamato, "A design of novel grooved circular waveguide polarizers," *IEEE Trans. Microw. Theory Techn.*, vol. 48, no. 12, pp. 2446–2452, Dec 2000.
- [12] S.-W. Wang, C.-H. Chien, C.-L. Wang, and R.-B. Wu, "A circular polarizer designed with a dielectric septum loading," *IEEE Trans. Microw. Theory Techn.*, vol. 52, no. 7, pp. 1719–1723, July 2004.
- [13] R. V. Gatti and R. Rossi, "A novel meander-line polarizer modeling procedure and broadband equivalent circuit," *IEEE Trans. Antennas Propag.*, vol. 65, no. 11, pp. 6178–6184, Nov 2017.
- [14] C. Molero, M. García-Vigueras, R. Rodríguez-Berral, F. Mesa, and N. Llombart, "Equivalent circuit approach for practical applications of meander-line gratings," *IEEE Antennas Wireless Propag. Lett.*, vol. 16, pp. 3088–3091, 2017.
- [15] C. D. Diallo, E. Girard, H. Legay, and R. Sauleau, "All-metal ku-band luneburg lens antenna based on variable parallel plate spacing fakir bed of nails," in *2017 11th European Conference on Antennas and Propagation (EUCAP)*, March 2017, pp. 1401–1404.
- [16] Q. Liao, N. J. G. Fonseca, and O. Quevedo-Teruel, "Compact multibeam fully metallic geodesic luneburg lens antenna based on non-euclidean transformation optics," *IEEE Trans. Antennas Propag.*, vol. 66, no. 12, pp. 7383–7388, Dec 2018.
- [17] P. Fei, Z. Shen, X. Wen, and F. Nian, "A single-layer circular polarizer based on hybrid meander line a loop configuration," *IEEE Trans. Antennas Propag.*, vol. 63, no. 1, pp. 4609–4614, Oct 2015.
- [18] S. M. A. Momeni-Hasan-Abadi and N. Behdad, "Wideband linear-to-circular polarization converters based on miniaturized-element frequency selective surfaces," *IEEE Trans. Antennas Propag.*, vol. 64, no. 2, pp. 525–534, Feb 2016.
- [19] L. Young, L. A. Robinson, and C. A. Hacking, "Meander-line polarizer," *IEEE Trans. Antennas Propag.*, vol. 21, no. 3, pp. 376–378, May 1973.
- [20] M. A. Joyal and J. J. Laurin, "Analysis and design of thin circular polarizers based on meander lines," *IEEE Trans. Antennas Propag.*, vol. 60, no. 6, pp. 3007–3011, June 2012.
- [21] M. A. Joyal, M. Riel, Y. Demers, and J. J. Laurin, "A meander-line circular polarizer optimized for oblique incidence," *IEEE Trans. Antennas Propag.*, vol. 63, no. 12, pp. 5391–5398, Dec. 2015.
- [22] M. Letizia, B. Fuchs, C. Zorraquino, J. F. Zcher, and J. R. Mosig, "Oblique incidence design of meander-line polarizer for dielectric lens antennas," *Prog. Electrom. Res. B*, vol. 45, no. 12, pp. 309–335, Feb. 2012.
- [23] J. Epis, "Broadband antenna polarizer," *US Patent 3 754 271*, Aug. 1973.
- [24] N. Marcuvitz, *Waveguide Handbook*. New York, USA: McGraw-Hill Book Company, 1951.
- [25] G. Pérez-Palomino, J. E. Page, M. Arrebola, and J. A. Encinar, "A design technique based on equivalent circuit and coupler theory for broadband linear to circular polarization converters in reflection or transmission mode," *IEEE Trans. Antennas Propag.*, vol. 66, no. 5, pp. 2428–2438, May 2018.
- [26] F. J. Vázquez-Sánchez, "Electromagnetic wave polarizer screen," *EP 2 469 653 A1*, Jun. 2012.
- [27] G. Collignon, "Polarisation device for a satellite telecommunications antenna and associated antenna," *US Patent 0372820 A1*, Dec. 2016.
- [28] G. F. Craven and C. K. Mok, "The design of evenness mode waveguide bandpass filters for a prescribed insertion loss characteristic," *IEEE Trans. Microw. Theory Techn.*, vol. 19, no. 3, pp. 295–307, Mar. 1971.
- [29] C. Molero, T. Debogovic, and M. García-Vigueras, "Design of full-metal polarizing screen based on circuit modeling," in *International Microwave Symposium (IMS)*, Philadelphia, USA, 2018.
- [30] F. Medina, F. Mesa, and R. Marqués, "Extraordinary transmission through arrays of electrically small holes from a circuit theory perspective," *IEEE Trans. Microw. Theory Techn.*, vol. 56, no. 12, pp. 3108–3120, Dec. 2008.
- [31] R. Rodríguez-Berral, F. Mesa, and F. Medina, "Analytical multimodal network approach for 2-d arrays of planar patches/apertures embedded in a layered medium," *IEEE Trans. Antennas Propag.*, vol. 63, no. 5, pp. 1969–1984, May 2015.
- [32] P. Rodríguez-Ulibarri, M. Navarro-Cía, R. Rodríguez-Berral, F. Mesa, F. Medina, and M. Beruete, "Annular apertures in metallic screens as extraordinary transmission and frequency selective surface structures," *IEEE Trans. Microw. Theory Techn.*, vol. 65, no. 12, pp. 4933–4946, Dec 2017.
- [33] R. Rodríguez-Berral, F. Mesa, and F. Medina, "Resonant modes of a waveguide iris discontinuity: Interpretation in terms of canonical circuits," *IEEE Trans. Microw. Theory Techn.*, pp. 1–11, 2018.
- [34] F. Mesa, M. Garca-Vigueras, F. Medina, R. Rodríguez-Berral, and J. R. Mosig, "Circuit-model analysis of frequency selective surfaces with scatterers of arbitrary geometry," *IEEE Antennas and Wireless Propag. Lett.*, vol. 14, pp. 135–138, 2015.
- [35] C. Molero, R. Rodríguez-Berral, F. Mesa, and F. Medina, "Dynamical equivalent circuit for 1-d periodic compound gratings," *IEEE Trans. Microw. Theory Techn.*, vol. 64, pp. 1195 – 1208, April 2016.